AIAA JOURNAL
Vol. 45, No. 12, December 2007

# High-Altitude Plume Simulations for a Solid Propellant Rocket

Jonathan M. Burt* and Iain D. Boyd†
*University of Michigan, Ann Arbor, Michigan 48109*

DOI: 10.2514/1.30129

**A simulation scheme is proposed for flowfield and radiation analysis of solid rocket exhaust plumes at high altitude. Several recently developed numerical procedures are used to determine properties of the gas and condensed phase $Al_2O_3$ particles, and spectrally resolved plume radiation calculations are performed using a Monte Carlo ray trace model. Simulations are run for a representative plume flow at 114 km, and a comparison is made with experimental measurements of ultraviolet radiance. A series of parametric studies involving simulations of this same flow are used to evaluate the influence of physical processes and input parameters related to gas–particle interaction, particle radiation, and the presence of soot.**

## I. Introduction

IN THE flowfield simulation and radiation analysis of solid rocket exhaust plumes at very high altitudes, a number of approximations and simplifying assumptions are typically made due to computational cost, a lack of existing models, or uncertainty over the influence of various physical phenomena. These flows tend to include a large mass fraction of $Al_2O_3$ particles, which can significantly influence bulk flow properties and dominate plume radiative emission through much of the infrared (IR), visible, and ultraviolet (UV) range. Some determination of particle-phase characteristics is typically required for useful and accurate simulation results and may be necessary to assess base heating rates, radiation signatures, surface contamination effects, or other flow properties of interest. As a result, important physical processes and phenomena associated with gas–particle interaction must be recognized and incorporated into simulation procedures. Several potentially important effects have received little attention in the literature, and the significance of coupling between many of these effects still remains an open question. In this paper, we attempt to address the uncertainty in the significance of various effects and describe a general procedure for the simulation of rarefied plume flows from solid-propellant rockets.

At very high altitudes (above roughly 100 km), solid rocket motor (SRM) exhaust gases typically experience a high degree of thermal nonequilibrium through much of the plume. As the exhaust gases rapidly expand beyond the nozzle exit, thermal energy is increasingly distributed nonuniformly among the translational and internal degrees of freedom, and the gas velocity distribution may deviate significantly from the equilibrium limit. This is particularly true around the nozzle lip, in the plume backflow region upstream of the nozzle exit plane, and in the plume–atmosphere interaction region where a thick mixing layer may be bounded on either side by highly diffuse shock waves [1]. Under these conditions, the quasi-equilibrium assumptions underlying most continuum computational fluid dynamics (CFD) methods break down and alternate simulation techniques valid for transitional flow regimes must be used. Additional procedures are required for inclusion of the $Al_2O_3$ particle phase, which consists of particles in both liquid and solid states with diameters ranging from roughly 0.1 to 10 $\mu$m, and which commonly accounts for 15–30% of the mass flow through the nozzle [2]. Momentum and energy exchange between particles and the surrounding gas may significantly influence properties of both phases, and the locally free-molecular nature of gas–particle interactions makes a kinetic theory approach more appropriate than traditional continuum methods for two-phase flow simulation. Coupling between radiative heat transfer and flowfield characteristics may also be important, because particle-phase emission and absorption can significantly affect properties of both the particles and gas.

In recent years, considerable work has been performed with the goal of advancing numerical modeling techniques for phenomena associated with SRM plume flows. Much of this work has focused on low to intermediate altitudes, for which gas flow simulation may be accurately handled by a continuum solver for the Navier–Stokes equations and for which condensed phase particles are uniformly much larger than the mean free path in the surrounding gas [3–5]. In higher-altitude plumes, significant gas thermal nonequilibrium and large particle Knudsen numbers necessitate an alternate simulation approach based on kinetic theory. However, until very recently, published modeling efforts for high-altitude SRM plume flows have involved large simplifications to the underlying flow physics. Simulations of Ratteni [6] and of Clark et al. [7] employ a method of characteristics calculation procedure that does not account for nonequilibrium phenomena in the gas. Simulations presented by Hueser et al. [8] neglect the influence of condensed phase particles, but use a more physically justified hybrid gas simulation scheme, in which the method of characteristics is used in near-equilibrium flowfield regions and the direct simulation Monte Carlo (DSMC) method [9] (valid for any Knudsen number regime for a dilute gas) is used elsewhere.

Additional simulations of Candler et al. [10], Anfimov et al. [11] and Vitkin et al. [12] involve significantly more complex physical models and include both two-way interphase-coupling effects and uncoupled plume radiation calculations. These simulations use a gas simulation approach based on the Navier–Stokes equations, which does not include translational nonequilibrium effects, and employ near-continuum approximations in gas–particle interaction models that may further reduce accuracy or generality of the simulation procedures.

In the last few years, a number of DSMC-based SRM plume simulation efforts [13–15] have largely eliminated near-equilibrium approximations related to gas flow characteristics and gas–particle interaction, due in part to the recent introduction of two-phase modeling procedures in DSMC [16]. In possibly the most ambitious such effort, a hybrid Navier–Stokes/DSMC simulation procedure is used to model the gas, and an uncoupled reverse Monte Carlo scheme is used for plume radiation analysis [17]. Although this last study examines a similar test case and includes many of the same models presented later, it leaves open a number of questions regarding the

Presented as Paper 1013 at the 45th AIAA Aerospace Sciences Meeting and Exhibit, Reno NV, 8–11 January 2007; received 30 January 2007; revision received 23 July 2007; accepted for publication 31 July 2007. 

*Postdoctoral Research Fellow, Department of Aerospace Engineering. Member AIAA.
†Professor. Associate Fellow AIAA.

influence of modeling parameters and approximations, which we address in the present work.

Over the course of a multiyear project, numerical modeling procedures have been developed for a number of potentially important phenomena associated with high-altitude SRM plume flows, and various models have been individually tested on simple test cases and subscale flows involving a freely expanding plume [18–21]. For the current effort, a number of these physical models are used together on a larger-scale, more complicated flow that better represents the plume flows of interest, and some limited comparison is made between calculated radiation characteristics and available experimental data. Additional simulations are performed for which individual models are disabled or input parameters are varied, in an effort to determine the importance of several physical processes and numerical approximations on flowfield and radiation properties. In the first of these parametric studies, we consider the sensitivity of flowfield and radiation properties to procedures for modeling momentum and energy exchange between condensed phase particles and the surrounding gas. Next, we consider the influence of procedures used in particle radiation modeling. Finally, the potential impact of soot particles on plume radiation properties is examined. Results are presented with the general goal of quantifying the influence and interaction of various phenomena so that less uncertainty over the importance of these phenomena may exist in future simulation efforts for similar flows.

## II. Numerical Procedures and Simulation Setup

For ease of comparison and to limit the required computer resources, experimental measurements are desired for a plume flow that can be modeled through an axisymmetric simulation. The exhaust flow should therefore be expelled through a single nozzle, and the rocket should be oriented at a small inclination relative to its direction of motion. To the authors' knowledge, the only experimental measurements for a single-nozzle high-altitude SRM plume flow in the open literature are those of Erdman et al. [22]. In a flight experiment named "Bow Shock Ultraviolet 2" (BSUV-2), onboard sensors were used to measure spectral radiance in the near-UV range (wavelengths of 0.2 to 0.4 $\mu$m) from upper-stage SRM exhaust plumes at altitudes between roughly 100 and 120 km.

The plume from the third-stage Star-27 SRM at an altitude of 114 km is used as a test case here, and although no experimental data are available on flowfield properties, we can, to a limited extent, infer overall simulation accuracy from a comparison of radiation characteristics between numerical and experimental results. Following previous simulations of Candler et al. [10] for the same flow, we perform a series of axisymmetric simulations on a rectangular grid that extends from 10 m upstream to 75 m downstream of the nozzle exit plane and 30 m radially outward from the nozzle centerline. The nozzle exit diameter is 0.78 m, and the rocket surface geometry is approximated as a blunted cone-cylinder shape of length 3.1 m. The grid boundary geometry is shown with relevant boundary condition types in Fig. 1.

To account for the high degree of gas thermal nonequilibrium expected through much of the grid domain, the direct simulation Monte Carlo (DSMC) method [9] is used as a basis for gas-property calculations. The variable-hard-sphere collision model is employed to approximate the variation in transport properties with temperature, and the Larsen–Borgnakke model [9] is used, together with a total collision energy model for the probability of inelastic collisions, to determine energy exchange between translational and rotational modes.

Because the gas density in much of the plume core region downstream of the nozzle is far too high to meet standard DSMC cell-size requirements on all but the largest parallel machines, an alternate approach for gas-phase simulation must be used in this region. The traditional collision-limiter approach provides a simple solution, but is considerably less efficient and arguably less accurate than alternate methods that involve resampling some fraction of representative gas-molecule velocities during each time step from predetermined

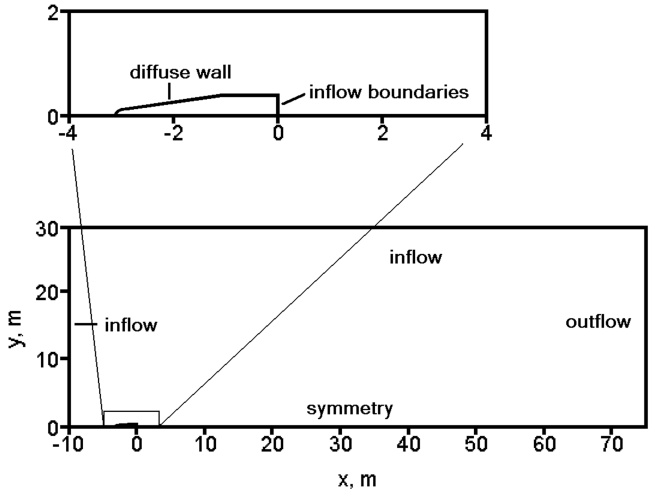


**Fig. 1 Grid geometry for simulations of the BSUV-2 flow.**

distribution functions. Both types of approaches can produce large artificial diffusion errors and tend to enforce a near-equilibrium gas velocity distribution that may not be physically justified when cell dimensions are much greater than a mean free path [23]. However, these approaches are generally far simpler to implement than alternate methods, such as hybrid CFD/DSMC algorithms, for simulating flowfields that include both continuum regions and nonequilibrium regions in which a DSMC calculation is desired. This is particularly true for simulations involving a large number of additional physical models or those for which strong two-way coupling may exist between continuum and nonequilibrium regions.

For this study, gas properties in the high-density, near-equilibrium, core flow region of the plume are calculated using a recently developed particle method based on the ellipsoidal statistical Bhatnagar–Gross–Krook (ES-BGK) equation [24]. Consideration is made for effects of moderate translational and rotational nonequilibrium, and an exact momentum and energy-conservation scheme is used to minimize random-walk errors. The location of the boundary between DSMC and ES-BGK domains is determined using a standard cutoff value (0.05) of the maximum gradient-length local Knudsen number [25]. This is a nondimensional continuum breakdown parameter defined as the maximum ratio of the local mean free path to characteristic length scales based on gradients in translational temperature, bulk velocity, or density, and it has been used in previous studies to estimate the validity of near-equilibrium simulation methods under a variety of conditions.

Condensed phase particles are included in the simulation here through a standard Lagrangian approach, in which representative particles are tracked through the grid and sorted into cells using procedures similar to those in DSMC. The momentum and energy transfer to a particle from the surrounding gas is computed using a method of Gallis et al. [16], based on assumptions of locally free-molecular flow and an approximation that all interphase collisions involve either specular reflection or diffuse reflection with full thermal accommodation to the particle temperature. In this deterministic model, each DSMC gas molecule assigned to the same cell as a simulated condensed phase particle represents a large spatially uniform collection of real gas molecules, some fraction of which collide with the particle and are either specularly or diffusely reflected. Analytical solutions for incident and reflected components of momentum and energy transfer are integrated over all potential collision points on the particle surface. The reciprocal momentum and energy transfer from a particle to the gas is determined through a probabilistic two-way coupling approach [18], which involves representative calculations for individual interphase collisions. Modifications to both methods are made to allow for nonspherical particles and to account for effects of particle rotation [19]. Collisions between condensed phase particles within the plume are neglected, based on a simplified analysis showing an extremely low maximum collision frequency.

A model for nonequilibrium crystallization of liquid $Al_2O_3$ droplets is implemented as well [20]. The crystallization model is based on finite rate phase-change approximations, in which a droplet is assumed to remain in a completely liquid state until its temperature drops below the nucleation temperature for homogeneous crystallization. (Note that the nucleation temperature, 1930 K, is considerably below the $Al_2O_3$ melting temperature of 2327 K.) A heterogeneous crystallization front then forms over the droplet surface and progresses toward the center of the solidifying particle at a temperature-dependent rate. Energy released during this process increases the particle temperature, whereas effects of phase composition on the particle material density and radiative properties are neglected. Further phase transitions between metastable and stable solid states are also not considered. The crystallization process for a given particle may occur over a large number of simulation time steps, and in contrast to equilibrium phase-change approximations, the particle will not maintain a uniform temperature during this period. A detailed description of the model is provided in [20].

Radiative heat transfer to and from the particles is calculated using a Monte Carlo ray trace (MCRT) radiation model, which involves tracking a large number of representative energy bundles through the computational domain. Energy bundles here represent a large collection of photons over some finite wavelength range and are created periodically at randomly selected source particles throughout the grid. Additional energy bundles are created along inflow boundaries at the nozzle exit, to account for effects of continuum "searchlight" emission from within the nozzle. This model is strongly coupled to the flowfield simulation and allows for spectrally resolved radiation calculations in an emitting, absorbing, and scattering medium of arbitrary optical thickness [21].

Following the simulations of Anfimov et al. [11], the $Al_2O_3$ particle phase is assumed to account for 30% of the mass flow at the nozzle exit and is made up of seven discrete particle sizes ranging from 0.3 to 6 $\mu$m in diameter. Properties for each particle size are independently specified along inflow boundaries at the nozzle exit plane. These inflow properties, as well as those of the gas, are taken from a nozzle flow simulation by Anfimov et al. Because of a lack of available flowfield information at the nozzle exit, most particle properties given by these authors are assumed uniform over the exit plane. The one exception is in the initial particle directions; for both particles and gas, the direction of bulk velocity vectors along the nozzle exit plane is set to vary linearly with distance from the axis. Particle trajectories and gas streamlines at the nozzle exit have no radial component along the axis and reach a maximum off-axis angle of 17.2 deg (equal to the nozzle divergence angle) at the nozzle lip.

A rough estimate of the initial solid mass fraction for each particle size is found by taking the difference between the nucleation temperature (1930 K) for homogeneous crystallization of $Al_2O_3$ and the assigned particle temperature, then multiplying this by the ratio of the specific heat (1225 J/kg · K) to the latent heat of fusion ($1.07 \times 10^6$ J/kg) for liquid $Al_2O_3$. This estimation procedure follows from energy-conservation arguments and an approximation that the solid mass fraction will be zero when the initial particle temperature is equal to the nucleation temperature. Based on this procedure and the initial particle temperatures given by Anfimov et al. [11], at the nozzle exit, the largest particles are in a completely liquid state and the smallest particles have a liquid mass fraction of 58%. Particle properties at the nozzle exit are given in Table 1, in which all values are either taken directly from the data of Anfimov et al. or are derived from this data, as described earlier.

**Table 1 Particle properties at the nozzle exit**

| Diameter, $\mu$m | Mass flux, kg/(m$^2$ · s) | Temperature, K | Speed, m/s | Liquid mass fraction |
|---|---|---|---|---|
| 0.3 | 0.0443 | 1562 | 2992 | 0.579 |
| 0.4 | 0.0367 | 1634 | 3051 | 0.661 |
| 0.6 | 0.133 | 1834 | 3023 | 0.89 |
| 1 | 0.592 | 2293 | 2973 | 1 |
| 2 | 2.29 | 1920 | 2855 | 0.989 |
| 4 | 7.53 | 2178 | 2674 | 1 |
| 6 | 1.84 | 2407 | 2472 | 1 |

The exhaust-gas species are limited here to the primary species $H_2$, $N_2$, and CO, with mole fractions at the nozzle exit of 0.38 for $H_2$ and 0.31 for both $N_2$ and CO. These mole fraction values are selected to give approximately the same molecular weight for the exhaust-gas mixture as that used in the simulations of Anfimov et al. [11]. Also following Anfimov et al., the gas is assigned a bulk speed of 3113 m/s, a temperature of 1433 K, and a density of 0.011 kg/m$^3$ along inflow boundaries at the nozzle exit. At atmospheric inflow boundaries shown in Fig. 1, the gas has mole fractions of 0.78 for $N_2$ and 0.22 for $O_2$, with a temperature of 288 K, a density of $5.79 \times 10^{-8}$ kg/m$^3$, and a freestream Mach number of 13.5. A thermal accommodation coefficient of 0.9 is used for collisions between gas molecules and $Al_2O_3$ particles, whereas the outer surfaces of the rocket are modeled as diffusely reflecting walls at 300 K with full thermal accommodation.

It should be noted that the initial conditions along the nozzle exit plane, for both the gas and $Al_2O_3$ particles, constitute a rough approximation of conditions expected in the actual exhaust flow. In particular, relatively little information is provided by Anfimov et al. [11] on the internal nozzle flow simulation used to determine many of the inflow quantities used here. These authors do, however, describe nozzle flow simulation procedures involving a numerical solution to the parabolized Navier–Stokes equations, with modifications for vibrational relaxation and two-way interphase coupling between the particles and gas. Because of approximations in the nozzle flow simulation and limitations in the published data, it can be argued that our use of this data may significantly reduce the overall accuracy of plume simulation results. The presumed lack of droplet breakup, agglomeration, and combustion modeling in the nozzle may introduce errors in flow quantities at the exit plane, and the assumption of uniform particle number density along the nozzle exit likely adds additional errors. However, our main goal here is to introduce a unified framework for external flowfield and radiation analysis and to evaluate the influence of physical models and simulation parameters in plume and atmospheric flowfield regions. These potential errors can therefore be tolerated, with the understanding that they may have some influence on simulation accuracy.

In the particle radiation model employed here [21], particle spectral emissivity values are assumed to scale with the ratio of the particle absorption index to the wavelength, following a correlation of Reed and Calia [2]. Absorption index values are in turn calculated as a function of temperature and wavelength. In the IR range in which most radiative energy transfer is concentrated, absorption index values are interpolated from experimental measurements of Konopka et al. [26], whereas those in the UV range are found using a series of correlations given by Anfimov et al. [11].

Calculations are run for about 60 h on eight 1.4-GHz AMD Athlon processors. Domain decomposition is used to roughly evenly divide the computational load among all processors, and cell size, time step, and numerical weights are carefully varied throughout the grid to balance overall simulation accuracy with computational efficiency. The unstructured grid is made up of about 87,000 triangular cells, through which around 7.5 million DSMC gas particles and 160,000 representative $Al_2O_3$ particles are tracked at steady state. Cell dimensions range from 0.01 m at the nozzle exit to 0.5 m along the atmospheric inflow and outflow boundaries shown in Fig. 1 and are varied through much of the grid, roughly in proportion to the local mean free path.

To assure grid convergence, a second simulation is run for which all cell dimensions are halved, for a total of four times as many cells, and a variety of flow property values are compared between the two sets of simulation results. The most sensitive of the properties considered (the gas translational temperature $T_t$) is found to vary by no more than a few percent between simulations using the original and refined grids. Values of $T_t$ for both simulations are plotted in Fig. 2 along a straight extraction line that runs from the midpoint along the nozzle exit radius to a point 75 m downstream and 25 m radially outward. This extraction line roughly follows the

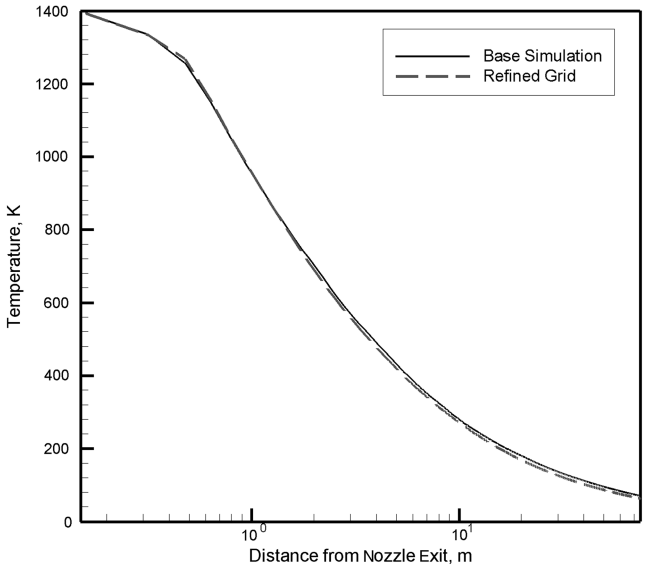


**Fig. 2 Gas translational temperature along the extraction line.**

gas streamline that passes halfway between the nozzle lip and central axis and is used in subsequent sections as a convenient measure for the variation of gas and particle properties through the plume.

## III. Simulation Results

Figure 3 presents a close-up view of gas bulk-velocity contours and streamlines in a 10-m-long region surrounding the rocket. The figure shows a highly diffuse bow shock, with a large boundary layer along the front portion of the rocket surface. Further downstream, a thick mixing layer forms along the region of plume–atmosphere interaction, and a small plume backflow region is found just upstream of the nozzle exit and within a few meters of the rocket. Within the plume, streamlines and velocity contours show the characteristics of a near-free expansion flow (including a complete absence of shocks), as expected for a highly underexpanded plume at very high altitude. Note the well-resolved boundary between the plume and atmospheric flow regions.

Contours of average particle temperature are shown in Fig. 4 for 0.4- and 4-$\mu$m-diam $Al_2O_3$ particles. Note first the difference in the regions occupied by particles of the two different sizes. Smaller particles experience a greater radial acceleration in the plume near-field region just beyond the nozzle exit, and so the maximum divergence angle is greater for the smaller particle size. Also note that the temperature of the smaller 0.4-$\mu$m particles is uniformly about

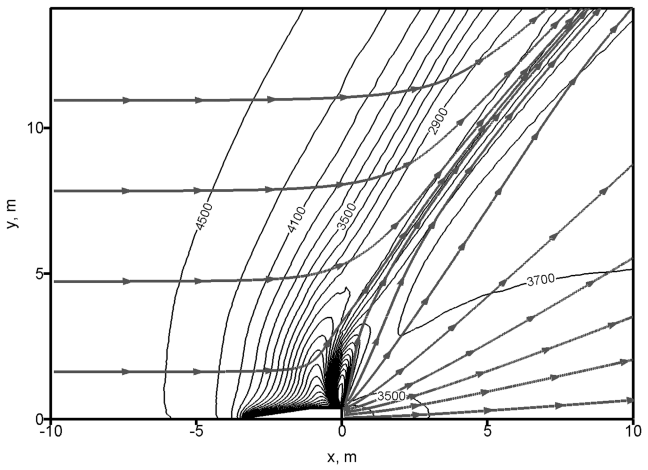


**Fig. 3 Gas streamlines and contours of bulk velocity magnitude; contour line values are given in m/s.**

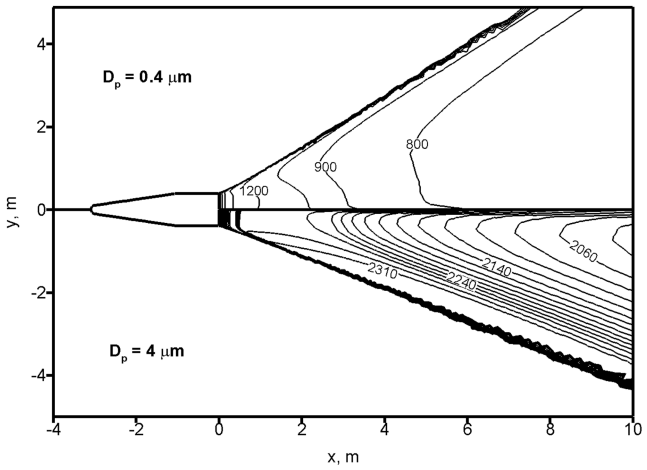


**Fig. 4 Close-up view of particle temperature contours; values are given in Kelvin.**

1200 K lower than that of the 4-$\mu$m particles. This can be explained by the dependence on the particle diameter $D_p$ for particle heat capacity, which scales as $D_p^3$, and the convective heat transfer rate, which is proportional to $D_p^2$. It follows from these scaling relations that the rate of change in particle temperature tends to vary as $1/D_p$ so that smaller particles will be more rapidly cooled by the surrounding gas in the plume near-field region where convective heat transfer is significant.

For both particle sizes in Fig. 4, the average temperature is generally found to increase with distance from the central axis. This is due to the fact that most trends in particle temperature are dominated by the influence of convective heat transfer. Because the convective heat transfer rate is proportional to the local gas density, we expect that particles that pass through the lower-density portions of the plume further from the axis will experience less heat loss to the cooler surrounding gas. Particles further from the axis will therefore retain higher temperatures, as is shown in the figure. The increase in particle temperatures at points very close to the axis is also related to the radial variation in gas density within the plume near-field region. Random-walk errors in cells near the axis produce an artificially low gas density, which in turn reduces convective heat transfer rates for particles that pass through these cells. (This random walk is a consequence of the near-axis reduction in numerical weights required to populate cells along the axis with a sufficient number of representative gas molecules.)

A close observation of 4-$\mu$m particle temperature contours in Fig. 4 reveals a rapid temperature jump about 0.4 m downstream of the nozzle exit. This jump is associated with the initiation of the phase-change process and results from the release of the latent heat of fusion for liquid $Al_2O_3$. As given in Table 1, 4-$\mu$m particles are assumed to be in a completely liquid state at inflow boundaries along the nozzle exit and are rapidly cooled by the surrounding gas until they reach the nucleation temperature for homogeneous crystallization. Once this temperature is reached, a radially symmetric crystallization front progresses from the surface of a particle toward its center. The heat release associated with the phase-change process causes a sudden increase in particle temperature, and this temperature increase in turn slows the progress of the crystallization front. For some time, a quasi-equilibrium state may be reached in which the heat release during crystallization is balanced by convective and radiative heat loss and the particle maintains a nearly uniform temperature. Further downstream, as the liquid mass fraction approaches zero and the rate of heat release is reduced, the particle temperature again begins to decrease, as observed in Fig. 4.

To demonstrate the correlation between phase change and the variation in particle temperatures, a contour plot of the liquid mass fraction for larger particle sizes is included here as Fig. 5. The top half of the figure shows cell-averaged liquid mass fractions for 4-$\mu$m particles, and the lower half gives contours for particles of 6-$\mu$m diameter. A comparison of characteristics for 4-$\mu$m particles

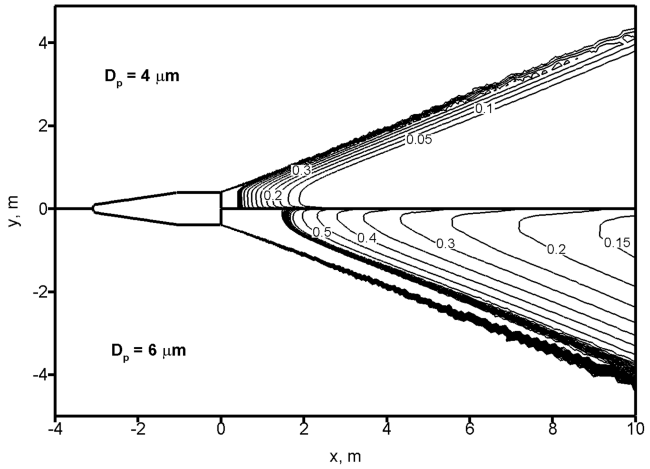


**Fig. 5 Contours of liquid mass fraction for 4- and 6-$\mu$m-diam particles.**

between Figs. 4 and 5 shows that, as described earlier, the particle temperature jump about 0.4 m downstream of the nozzle exit is accompanied by the initiation of phase change and a rapid reduction in the liquid mass fraction. Particle temperatures level off further downstream as the gradient in the liquid mass fraction decreases, and the particles ultimately approach a completely solid state.

In comparing liquid mass fraction contours for the two different particle sizes shown in Fig. 5, we find that phase change begins significantly further downstream for the larger 6-$\mu$m particles. As explained earlier, the rate of temperature decrease due to convective heat transfer tends to vary as roughly the inverse of the particle diameter, and so larger particles will experience a longer residence time in a completely liquid state before reaching the nucleation temperature at which crystallization may begin.

For both 4- and 6-$\mu$m particles, the onset of crystallization is shown in Fig. 5 to occur progressively downstream for particles that move along trajectories further from the axis. As with the radial variation in particle temperatures, this trend is a result of the decrease in gas density with distance from the axis. Particles that pass through regions of lower gas density will cool more slowly through convective heat transfer, and so these particles tend to reach the nucleation temperature at points further downstream.

In Fig. 6, contours are shown for the direction-averaged spectral radiative energy flux $E_\lambda$ at wavelengths of 2.2 and 0.24 $\mu$m. This flux is defined as the energy transfer rate per unit wavelength from photons within a narrow wavelength range that impinge on a spherical surface, divided by the cross-sectional area of the sphere. Although $E_\lambda$ values have little physical significance outside of the MCRT radiation model [21] used in the simulation, contours of $E_\lambda$ provide a convenient means of quantifying the variation in spectrally resolved radiation intensity throughout the simulated flowfield. The upper half of Fig. 6 can therefore be viewed as a measure of IR radiation intensity through the grid, and the lower half shows the intensity at a representative wavelength in the UV range. In comparing $E_\lambda$ contours for the two different wavelengths, we find that the IR radiation intensity is consistently about four orders of magnitude greater than the UV intensity, as follows from the fact that thermal radiative emission at the particle temperatures shown in Fig. 4 is typically concentrated in the IR range [2].

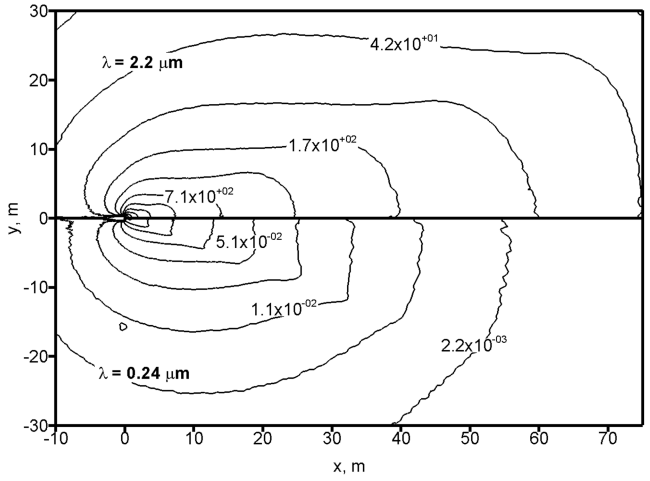


**Fig. 6 Contours of the direction-averaged spectral energy flux at wavelengths of 2.2 and 0.24 $\mu$m; values are in W/(m$^2$ · $\mu$m).**

A significant difference is also found in the shape of contour lines between the two wavelengths shown in Fig. 6. This difference may be attributed to the variation with wavelength in the temperature dependence for thermal emission. At smaller wavelengths, the spectral emissive power for a blackbody tends to depend far more strongly on the temperature of the body [27]. This characteristic is preserved in the procedures used to determine emissive power output for source particles in the radiation model [21]. As observed in Fig. 4, particles further from the axis tend to have higher temperatures so that they experience a greater rate of radiative heat loss. This temperature difference has a stronger correlation to emissive power in the UV range than in the IR range, and so a more pronounced ridge is shown in the UV energy-flux contours near the location of higher-temperature particles.

As shown in Fig. 6, the energy flux for both wavelengths is greatest at the nozzle exit, due primarily to the corresponding maximum in particle mass density and a reduction in the intensity of nozzle searchlight emission [21] with distance from the nozzle. Particles are modeled here as volumetric emitters [2,21] so that the magnitude of radiative fluxes should scale roughly with the local particle mass density. As this density decreases with downstream distance due to the divergence of particle trajectories through the plume, a continuous reduction in radiative energy flux is found in the axial direction.

A reduction in radiative energy flux is also observed in the radial direction, particularly outside the region where particles are found. This follows from the fact that in an axisymmetric simulation, the ratio of cell volume to the projected area on the grid will scale with distance from the axis. The average number of energy bundles that pass through a cell is proportional to the projected area of that cell in the grid plane, and the contribution of each bundle to the energy flux is proportional to the inverse of the cell volume. We therefore expect the net energy flux through cells outside the particle domain to scale approximately with the inverse of the distance from the axis, as is shown for both IR and UV wavelengths in Fig. 6.

## IV. Comparison with Experiment

Although there are no experimental measurements of flowfield properties that could be used to evaluate the overall accuracy of the simulation, some comparison can be made with experimental data and previous numerical results for radiation properties in the plume. In the BSUV-2 experiment [22], an onboard radiometer was used to measure UV spectral radiance along a downstream line inclined 4 deg to the nozzle centerline. The MCRT radiation model employed here is used to generate corresponding radiance values at several discrete wavelengths, and a comparison between numerical and measured values is shown in Fig. 7. Data points in the figure labeled "base simulation" are taken as the averages among eight otherwise identical simulations for which the random number generator is initialized at different points. The error bars give 95% confidence intervals based on a wavelength-averaged variance from the eight simulations and show that the stochastic nature of the radiation model produces significant scatter in these radiance values.

Published numerical results of Candler et al. [10] and Anfimov et al. [11] are also included in Fig. 7 for comparison. Both of these previous simulations employ continuum CFD methods that may be less appropriate for this flow than the kinetic approach used here, particularly in the highly rarefied regions upstream of the nozzle exit. Still, somewhat better agreement is found with experiment for these results than for those from the present simulations, particularly at

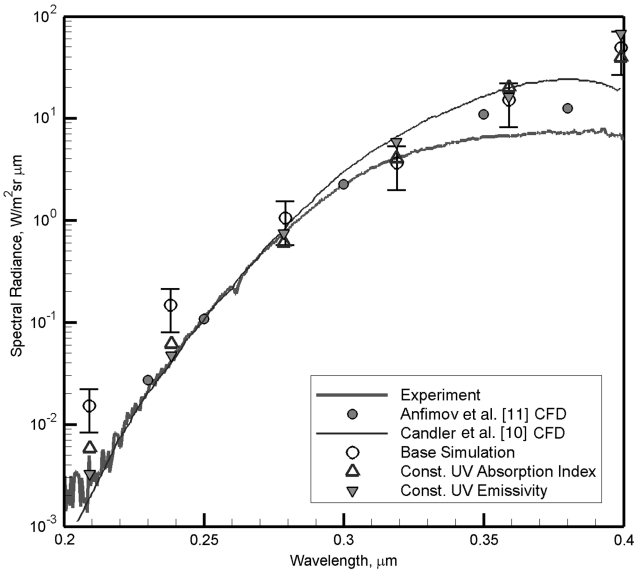


**Fig. 7 UV spectral radiance measured at the onboard sensor.**

wavelengths below around 0.25 $\mu$m. Note, however, that in the simulations of Candler et al. [10], particle-phase enthalpies at the nozzle exit were selected for best agreement between calculated and experimental radiance values at the 0.23-$\mu$m wavelength. This procedure effectively rescales the UV radiance profile to match experimental results and reduces the utility of any quantitative comparison with experiment.

In comparing the level of agreement between the different sets of results, also note that radiance values computed by Anfimov et al. [11] are subject to uncertainty associated with correlations for the particle absorption index introduced by these same authors. The correlations exhibit a strong temperature and wavelength dependence that has not been verified elsewhere in the literature, and they do not account for extrinsic properties (such as impurity concentrations and lattice defects) that have been found to dominate radiation characteristics of solid-phase $Al_2O_3$ particles [2]. Because the same correlations are employed for the simulations presented here, the resulting uncertainty in radiance values for both the new simulations and those of Anfimov et al. [11] leads to some doubt regarding the validity of using these values to assess overall simulation accuracy.

To determine the effect of the UV absorption index correlations on radiance values, two additional simulations are performed. In the first simulation, the absorption index is given a constant value of 0.01 through the UV range. This value is chosen to roughly characterize an average of values taken from the correlations of Anfimov et al. [11] over a range of temperatures and wavelengths. In the second simulation, the UV absorption index is set so that the spectral emissivity $\varepsilon_\lambda$ in the UV range is approximately constant. It follows from the correlation of Reed and Calia [2] that for a constant emissivity, the absorption index $k$ in this range must be proportional to the wavelength $\lambda$. For a given particle radius $R_p$, we can relate $k$ to $\lambda$ by

$$k = \frac{\varepsilon_\lambda \cdot \lambda}{4R_p} \tag{1}$$

Particles are modeled through Eq. (1) as volumetric emitters [2] so that in an isothermal enclosure containing particles with a range of sizes, the emissive heat flux per unit volume will scale with the mean-cubed particle radius. Because this flux should also scale with the average over all particle sizes of the quantity $\varepsilon_\lambda R_p^2$, an effective emissivity that is independent of the particle radius must be proportional to the ratio of the mean-cubed radius to the mean-squared radius. This ratio is equal to one-half the Sauter mean diameter, which may be substituted for $R_p$ in Eq. (1) for use with an effective emissivity that is independent of particle size.

Thus, to allow for values of the UV absorption index that give a uniform effective emissivity, we assume a characteristic Sauter mean diameter of 3.2 $\mu$m (as is found through much of the plume region occupied by particles) and use an emissivity of 0.2. From Eq. (1), this corresponds to the relation $k = 0.031\lambda$. The resulting $k$ values for this "constant-emissivity" case are generally of the same order as those found through the correlations of Anfimov et al. [11] and differ little from values used in the simulation involving a constant absorption index.

Radiance values from both additional simulations are shown in Fig. 7 and exhibit significantly better agreement with the experiment than do base simulation results. In particular, the constant-emissivity simulation gives excellent agreement with the experimental data at smaller wavelengths, in which the correlations of Anfimov et al. [11] produce the greatest disagreement. Although the choice of constant emissivity or absorption index values is to some extent arbitrary, the resulting consistency with experiment gives us reasonable confidence in the overall accuracy of the simulations.

## V. Sensitivity to Gas–Particle Interaction Models

The simulations presented here involve a large number of modeling procedures, which cover a range of physical phenomena and for which the sensitivity of simulation results to input parameters may not be known. The importance of coupling between the various models is also generally uncertain, and assumptions underlying several of these models may not always be valid under relevant flowfield conditions. Because the choice of input parameters and modeling approximations is of great importance in assessing the overall accuracy of the simulation approach, some evaluation is desired for the relative contributions and interactions among modeling procedures used in the simulations. For this evaluation, results from the base simulation described earlier are compared with those from a series of simulations for which individual models are turned off or input parameters are varied. The first category of physical models and numerical approximations to be assessed are those involved in momentum and energy exchange between the particles and gas.

First, the influence of momentum and energy coupling from particles to the surrounding gas is considered by deactivating the two-way interphase-coupling model [18], then performing a simulation for which gas properties are not affected by the presence of the particle phase. The effects of particle rotation are considered next, through the use of models for the exchange of angular momentum, linear momentum, and energy between a rotating sphere and a locally free-molecular nonequilibrium gas [19]. Particle angular velocities at the nozzle exit are given random directions along a plane normal to the nozzle centerline and are assigned magnitudes based on an estimate of the maximum angular velocity that avoids centrifugal breakup in liquid $Al_2O_3$ droplets. (Details of the procedure are provided in [19].) These droplets are assumed to rotate as a result of off-center coalescing collisions within the combustion chamber and nozzle.

Another property considered here is the influence of particle shape: Although $Al_2O_3$ particles extracted from SRM exhaust flows have been found to be roughly spherical, some authors have discussed an expected deviation of particle shapes from a perfect sphere due to surface forces on a solidifying droplet [2]. To quantitatively evaluate effects of particle shape, a simulation is performed for which particles are assumed to have the same surface-area-to-volume ratio as a cube. Following a detailed analysis of momentum and energy transfer rates between a rotating nonspherical particle and a locally free-molecular gas [18], the effective particle diameter and material density are modified to approximate the influence of a cube-shaped surface. Although this represents a deviation from spherical shape well out of the expected range, a comparison with base simulation results can be used to determine outer bounds for the influence of particle shape on various flowfield properties.

A final characteristic of gas–particle interaction considered here is the effect of the thermal accommodation coefficient (TAC) at the

particle surface. For all simulations described earlier, the particle TAC is set to 0.9 so that 90% of interphase collisions involve diffuse reflection with full accommodation to the particle temperature and the remaining 10% involve specular reflection. Although this TAC value is within the general range observed experimentally, the phenomenological nature of the collision model and a potentially strong dependence on surface and gas properties lead to some uncertainty over what value would be most appropriate. To assess the influence of the TAC value on flowfield properties, an additional simulation is performed for which the TAC is set to 0.45 so that interphase collisions are half as likely to involve diffuse reflection as in the base simulation.

Results from these simulations are compared by evaluating various flowfield properties along a straight extraction line that roughly follows the gas streamline originating midway between the nozzle lip and the intersection of the central axis with the nozzle exit plane. In the coordinate system of Fig. 1, the extraction line extends from the points $x = 0$ and $y = 0.2$ to $x = 75$ and $y = 25$, where all values are in meters. This is the same extraction line described in Sec. II for use in the grid convergence study. Results are shown in Figs. 8–12.

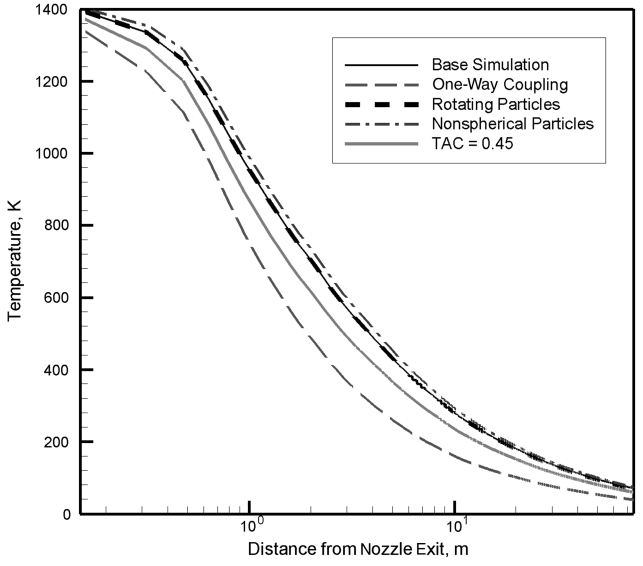


**Fig. 8 Gas translational temperature along the extraction line.**

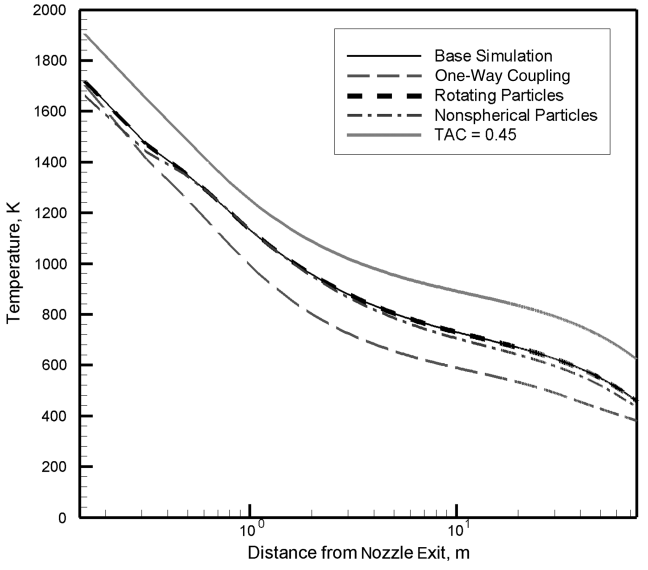


**Fig. 9 Temperature variation along the extraction line for 0.4-$\mu$m particles.**

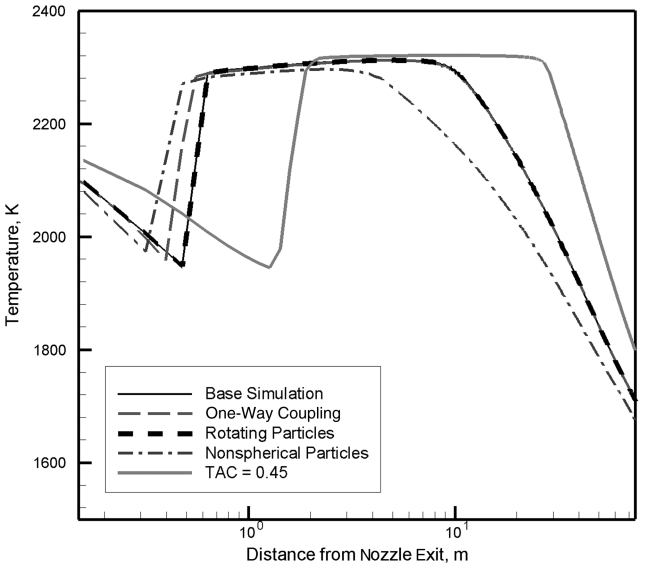


**Fig. 10 Temperature variation along the extraction line for 4-$\mu$m particles.**

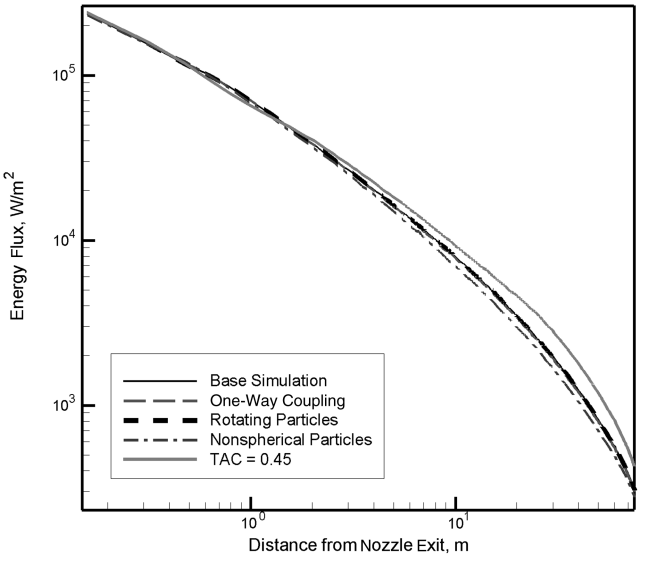


**Fig. 11 Net radiative energy flux along the extraction line.**

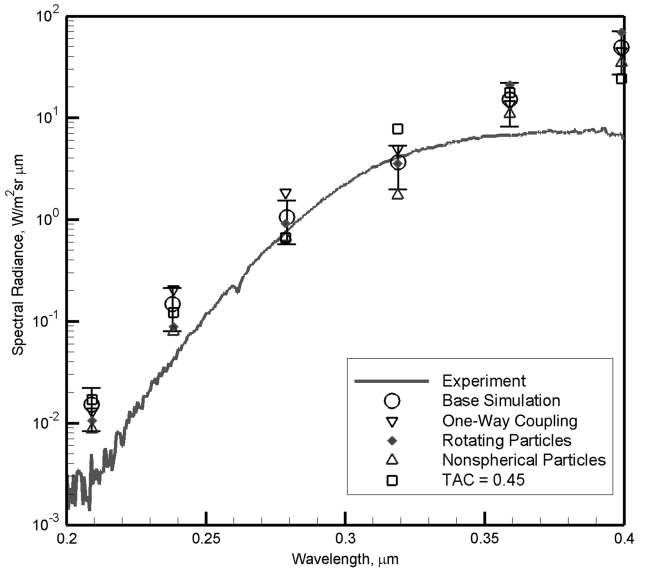


**Fig. 12 UV spectral radiance at the onboard sensor.**

In Fig. 8, the gas translational temperature for each of the simulations described earlier is plotted as a function of distance from the nozzle exit along the extraction line. The temperature variation for the base simulation shows generally expected trends for a plume flow expanding into a near-vacuum: The largest temperature gradient occurs in the near-field region just downstream of the nozzle exit, following a rapid conversion of thermal energy into bulk kinetic energy within this region. The rate of change slowly decreases with downstream distance as collisional processes become progressively less significant, and the translational temperature asymptotically approaches a far-field value near 0 K. Note that effects of rotational freezing allow for a potentially much higher asymptotic rotational temperature.

In comparing results with those from the base simulation, the one-way-coupling case is found to give significantly lower gas translational temperatures, particularly within the near-field plume region close to the nozzle exit. When the heat transfer from $Al_2O_3$ particles to the cooler surrounding gas is neglected, the gas temperature may be reduced within this region by well over 100 K. In contrast, the effect of particle rotation is found here to be negligible, because the gas temperature is shown to be nearly identical between the base simulation and the simulation for which particles leave the nozzle with maximum possible angular velocities.

Particle shape is shown in Fig. 8 to have a potentially measurable, although small, influence on gas temperatures through much of the plume. When particles of fixed mass are given greater surface area, the interphase collision frequency will increase and higher gas temperatures will result from a corresponding rise in convective heat transfer rates between the particles and gas. The simulation for which the particle TAC is set to 0.45 also gives translational temperature values noticeably different from those of the base simulation. When the probability that an interphase collision involves diffuse reflection is halved, the heat transfer rate between the particles and gas will be reduced by roughly 50% and particles will be considerably less effective in heating the surrounding gas. As a result, the gas translational temperature is found to decrease by up to approximately 50 K when the TAC is varied from 0.9 to 0.45.

Average temperatures along the extraction line for 0.4-$\mu$m-diam particles are shown in Fig. 9. The temperature plot for the base simulation shows a rapid drop in temperature around the nozzle exit and a temperature gradient that decreases continuously with downstream distance. An inspection of heat transfer rates shows that the downstream reduction in particle temperatures occurs primarily as a result of convective heat transfer in the near-field plume region within about 5 m of the nozzle exit, whereas radiative heat transfer dominates further downstream. In comparing results between the base simulation and the one-way-coupling simulation, for which effects on the gas of interphase momentum and energy exchange are neglected, we find trends similar to those described earlier for the gas temperature. Because the gas temperature is uniformly lower when one-way coupling is assumed and particles are unable to heat the surrounding gas, the local temperature difference between particles and gas will increase. A larger temperature difference corresponds to a greater convective heat transfer rate, and so particles will cool more rapidly and maintain lower temperatures, as is shown in the figure.

As with gas temperatures, the temperature of 0.4-$\mu$m particles is found to be almost completely unaffected by particle rotation. Particle temperatures are, however, shown to decrease slightly when given a nonspherical shape. Nonspherical particles will have a larger average collision cross section than spherical particles of equal mass so that they will cool more rapidly as a result of convective heat transfer. Note that as mentioned in the discussion of Fig. 6, particles are modeled as volumetric emitters, and so particle shape will have no effect on radiative heat transfer rates other than that associated with the difference in temperatures shown in Fig. 9. From the temperature plot for the simulation in which TAC = 0.45, we find that the TAC value significantly influences 0.4-$\mu$m particle temperatures throughout the plume. As a result of the roughly 50% reduction in convective heat transfer rates for this simulation, the temperature of 0.4-$\mu$m particles is found to be uniformly about 100 K higher than in the base simulation.

Figure 10 shows the variation along the extraction line in average temperatures for 4-$\mu$m-diam particles. The near-field temperature jump observed for all simulations here is a consequence of the nonequilibrium crystallization process, as explained earlier in the discussion of Figs. 4 and 5. A comparison between the base simulation results in Fig. 10 and those from the other simulations shows some surprising characteristics: When the TAC is reduced, convective heat transfer rates decrease and the location at which phase change begins is moved further downstream. Although this results in higher particle temperatures in the far-field plume region, the delay in phase-change initiation leads to significantly lower particle temperatures in a small region upstream of the temperature spike. This region, in which a lower TAC corresponds to reduced particle temperatures, is shown in the figure at locations between 0.5 and 1.1 m from the nozzle exit. Likewise, the increase in convective heat transfer rates associated with both nonspherical particles and an assumption of one-way coupling tends to force the phase-change initiation point upstream. Note, however, that the one-way-coupling simulation gives far-field particle temperatures nearly identical to those from the base simulation, whereas particle shape effects are found to be potentially significant throughout the plume.

As in Figs. 8 and 9, particle rotation is shown in Fig. 10 to have no noticeable effect on 4-$\mu$m particle temperatures. This is in fact true of all flowfield characteristics considered, and so we can conclude that particle rotation can generally be neglected in simulations of similar SRM plume flows, with no impact on simulation results. This conclusion is, however, subject to assumptions regarding the mechanisms by which particles develop angular momentum. If collisions involving partially or fully solidified particles are considered, then the appropriate value of the maximum angular velocity magnitude may be far higher. Higher angular velocities may also result from consideration of the interaction between solid particles and either nozzle walls or large-scale turbulent structures within the nozzle.

Figure 11 shows the variation in the net direction-averaged radiative energy flux along the extraction line. This flux is defined as the integral of the spectral radiative energy flux, displayed in the contour plots of Fig. 6, over the entire wavelength range (0.2 to 4.5 $\mu$m) considered in the radiation model. As described in the discussion of Fig. 6, the radiative energy flux is found to decrease continuously with downstream distance through the plume, primarily as a result of the divergence of particle trajectories. The greatest variation from base simulation results is observed for the simulation with TAC = 0.45, for which the energy flux through much of the far-field plume region is significantly higher. Much of this increase can be attributed to the difference in temperatures for 4-$\mu$m particles between the two simulations. These particles are shown in Fig. 10 to experience the greatest temperature difference about 25 m downstream of the nozzle exit. This location corresponds nearly exactly to the point in Fig. 11 at which the maximum difference in energy flux is observed. Because 4-$\mu$m particles make up roughly 60% of the total $Al_2O_3$ mass in the plume, and because the net emissive heat transfer rate increases with particle temperature, this correlation between trends shown in Figs. 10 and 11 is both logical and expected.

A similar correlation between the two figures is observed in comparing results for the base simulation and the simulation involving nonspherical particles. Spherical particles of 4-$\mu$m diameter are found in Fig. 10 to maintain significantly higher temperatures through much of the plume than nonspherical particles of equal mass. This temperature difference corresponds to a noticeable reduction in the radiative energy flux when nonspherical particles are used. In contrast, simulations involving one-way interphase coupling and rotating particles are both shown in Fig. 11 to give energy-flux values that are, within the scale of the figure, identical to those taken from base simulation results.

Note in Fig. 10 that the variation in TAC has a significant effect on 4-$\mu$m particle temperatures in the near-field plume region within a few meters of the nozzle exit, although no similar effect is found on energy-flux values in this region. Near-field differences in the temperature of 4-$\mu$m particles when two-way coupling is disabled or

when nonspherical particles are employed are also not reflected in Fig. 11. The lack of a correlation here between particle temperatures and energy flux is likely due to some combination of factors: First, smaller particles cool more quickly than larger 4-$\mu$m particles so that the relative influence of smaller particles on radiative energy flux will be greater at locations further upstream. Second, the net radiative energy flux at any point in the flowfield is a function of particle temperatures throughout the plume, and so contributions to the energy flux associated with large temperature variations in the near-field plume region will to some extent be smoothed out over the length of this region. Finally, nozzle searchlight emission [21] is expected to have a significant influence on the energy flux near the nozzle exit, and so $Al_2O_3$ particle emission will have a comparatively smaller effect on flux values here than at locations further downstream.

In Fig. 12, UV spectral radiance values at the onboard sensor are shown for the base simulation and for all simulations for which gas–particle interaction models are varied. The measured UV radiance profile from the BSUV-2 flight experiment is also included here for reference. Ideally, a comparison of radiance values from these simulations would give us some insight as to which numerical approximations and assumptions contribute most significantly to the discrepancy between simulation and experimental results. However, no clear trends are observed among the calculated radiance values, and through most of the wavelength range shown here, the variation between results from the different simulations is within the level of statistical uncertainty given by the error bars. We can at least conclude from this comparison that none of the modeling assumptions evaluated in this section are alone responsible for the discrepancy between experimental and calculated UV radiance profiles.

## VI. Influence of Radiation Modeling Parameters

In addition to numerical approximations and assumptions used for gas–particle interaction, overall simulation accuracy is subject to a number of approximations in the MCRT radiation model. To assess the influence of radiation modeling procedures on flowfield properties and on the plume radiation signature, further simulations are performed for which elements of flowfield radiation coupling are disabled or input parameters for the radiation model are modified.

First, the influence of radiative absorption is neglected by modifying the code so that MCRT energy bundles have no influence on the temperature of particles assigned to cells through which the energy bundles pass. This in effect decouples radiative absorption calculations from the flowfield simulation. Next, a simulation is run using the traditional postprocessing approach to plume radiation analysis, in which all radiative terms are neglected in the particle energy balance.

Results from additional simulations are used for comparison, to determine the influence of particle absorption index values on flowfield characteristics. In one simulation, an alternate set of IR absorption index values from the measurements of Konopka et al. [26] are used. These values are generally about one order of magnitude lower than those used in the base simulation. The inclusion of both data sets should allow for evaluation of the sensitivity of simulation results to the large inherent uncertainty in $Al_2O_3$ IR absorption index values. (As discussed by Konopka et al. and by Reed and Calia [2], this uncertainty is in part a consequence of an extreme sensitivity to small impurity concentrations, phase composition, and lattice defects in solid $Al_2O_3$.) Results are also considered from the two simulations discussed earlier for which the UV absorption index or spectral emissivity values are assumed independent of both temperature and wavelength.

Two additional simulations are also included here for comparison. In the first of these, an anisotropic scattering model [21] employed in all other cases is disabled and, instead, isotropic scattering is assumed. This procedure is equivalent to resetting the average cosine of the scattering angle in the Henyey–Greenstein scattering phase function from 0.5 (as taken from Reed et al. [28] and used in the other simulations) to zero. In the second simulation, the effect of

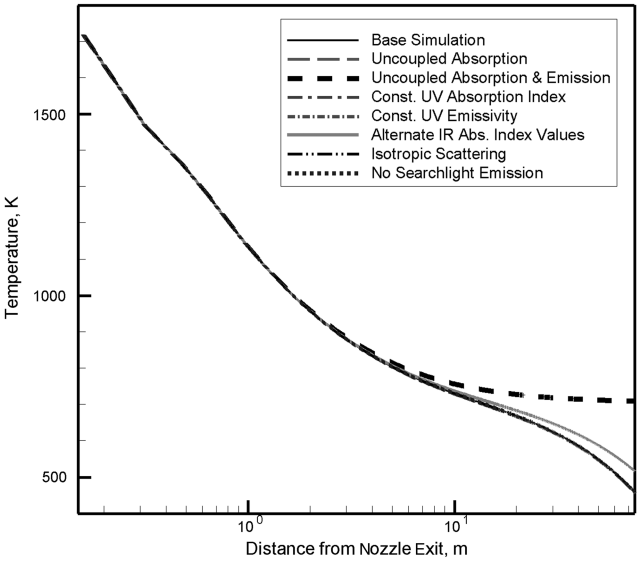


**Fig. 13 Temperature of 0.4-$\mu$m particles along the extraction line.**

continuum radiation (termed *searchlight emission*) from the interior of the nozzle is neglected so that all energy bundles used for radiation calculations originate at source particles within the interior of the grid.

In Fig. 13, temperatures for 0.4-$\mu$m-diam particles along the extraction line are compared among all simulations for which radiation modeling parameters are varied. The corresponding temperature plot for 4-$\mu$m particles is shown in Fig. 14. Note first that every modification to the radiation model described earlier has virtually no effect on particle temperatures in the plume near-field region within a few meters of the nozzle exit. Here, the particle energy balance is dominated by the influence of convective heat transfer, and particle residence time in this region is too small for emissive heat loss to have any significant cumulative effect. Any changes to radiation input parameters or modeling approximations should therefore have no impact on particle temperatures in the near-field plume region, as is observed in Figs. 13 and 14.

In comparing temperatures of both 0.4- and 4-$\mu$m particles between the base simulation and those for which elements of flowfield radiation coupling are disabled, we find that radiative absorption has no significant effect on particle temperatures, even in the far-field plume region toward the downstream edge of the simulation domain. In contrast, particle temperatures in this region

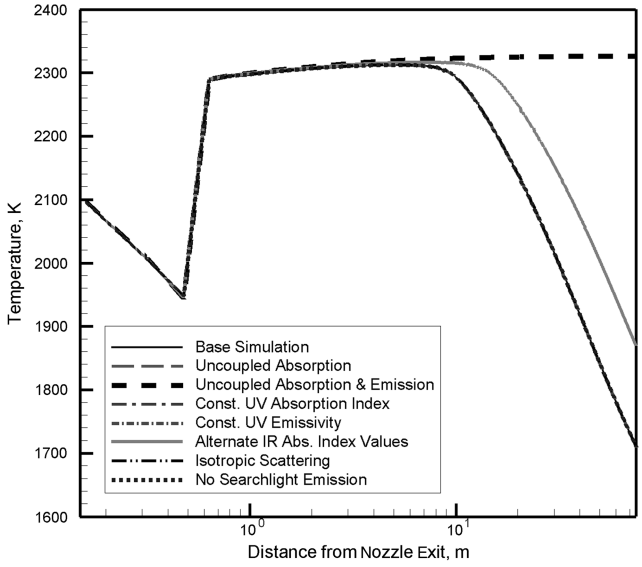


**Fig. 14 Temperature of 4-$\mu$m particles along the extraction line.**

may increase considerably when the contribution of emissive heat transfer is neglected.

When full radiation-flowfield coupling is included and IR absorption index values are reduced by roughly an order of magnitude to the alternate values of Konopka et al. [26], the far-field temperatures for both small and large particles are shown in Figs. 13 and 14 to increase significantly. Based on the findings of Konopka et al. that the difference between initial and reduced absorption index values represents the typical uncertainty in the IR absorption index range for $Al_2O_3$ particles in a SRM plume flow, we can assume that the difference between temperature curves for the base simulation and the simulation with alternate IR absorption index values corresponds to an unavoidable error margin in the results.

In contrast, the use of alternate absorption index values in the UV range produces no significant change in particle temperatures, due to the relatively small contribution of UV emission to the total radiative heat transfer rate. Results from the simulations in which anisotropic scattering or searchlight emission are neglected also appear nearly identical to those from the base simulation. Both searchlight emission and the angular dependence of scattering probabilities are therefore found to have no significant influence on the temperature of 0.4- and 4-$\mu$m-diam particles throughout the plume.

Values of the net radiative energy flux are shown in Fig. 15 for all simulations involving modifications to the radiation model. Note first that no difference is observed between results from the base simulation and those from the simulation in which the influence of radiative absorption on flowfield properties is neglected. However, a lack of radiation-flowfield coupling for both absorption and emission is found to significantly increase energy-flux values far downstream of the nozzle, as results from the corresponding increase in particle temperatures shown in Figs. 13 and 14.

The choice of values for the IR particle absorption index is found to significantly influence energy-flux values through the entire plume. When the lower "alternate" values are used, the net energy flux is considerably reduced in both near-field and far-field plume regions. This is due to the fact that thermal radiative emission in the relevant temperature range for $Al_2O_3$ particles occurs primarily at IR wavelengths. Because spectral emissivity is assumed in the radiation model to scale linearly with the absorption index, any large change to IR absorption index values will result in a comparable change to values of the net radiative energy flux.

We find no significant difference in the net energy flux when UV absorption index values are varied, because a relatively small fraction of emissive heat loss occurs in the UV range. A similar lack of influence on the energy flux is found in the scattering model; results shown in Fig. 15 for the simulation with isotropic scattering are virtually identical to those for the base simulation.

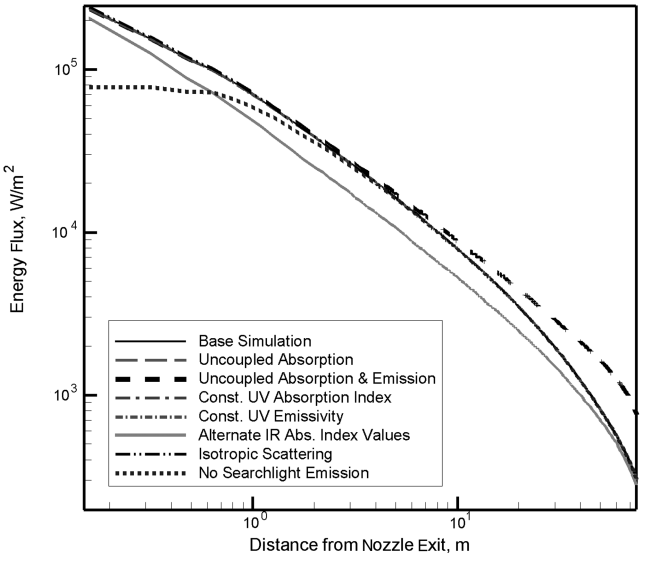


**Fig. 15 Variation along the extraction line in the net direction-averaged radiative energy flux.**

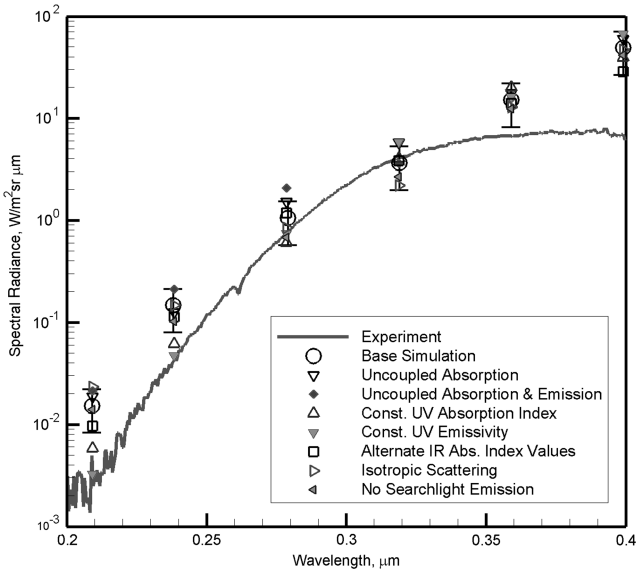


**Fig. 16 Dependence of UV spectral radiance on radiation model parameters.**

Nozzle searchlight emission is observed in Fig. 15 to account for over 50% of the net radiative energy flux around the nozzle exit, while providing a negligible contribution to flux values at distances greater than a few meters from the nozzle. Much of the downstream reduction in the radiative energy flux within the plume near-field region can be attributed to the corresponding decrease in the intensity of radiation emitted inside the nozzle. When nozzle searchlight emission is disabled, a far more gradual downstream reduction in energy flux is found in this region.

Figure 16 shows values of UV spectral radiance at the onboard sensor for all simulations described in this section, and data points from the BSUV-2 flight experiment are plotted for comparison. As mentioned in the discussion of Fig. 7, when either the UV absorption index or emissivity is assumed to be independent of wavelength, significantly better agreement is found with experimental radiance values in the 0.2- to 0.25-$\mu$m range, in which a particularly large discrepancy is observed between experimental values and those from the base simulation. The simulation for which both emission and absorption are uncoupled from flowfield calculations shows consistently higher radiance values than most other simulations, which results from the corresponding increase in particle temperatures.

The level of statistical scatter in Fig. 16 is great enough that few definite conclusions can be drawn from any trends observed in the figure. We do find, however, that of all the modifications to the radiation model considered here, only adjustments to the UV absorption index produce a statistically significant effect on calculated UV radiance values. It follows from this comparison that most other modifications to the radiation model cannot be assumed to measurably improve overall simulation accuracy, to the extent that simulation accuracy is established by the level of agreement between experiment and simulation results. Note that no broad conclusions can be drawn here for the general application of the radiation model to high-altitude SRM plume flows. If, for example, a much larger-scale plume of greater optical thickness had been considered, we expect that modifications to the scattering model would have a far more significant effect on the calculated radiance. The influence of both the scattering model and searchlight emission would also likely be much greater if the sensor field of view was aligned more closely to the nozzle exit plane [28].

## VII. Potential Influence of Soot on Plume Radiation

In addition to condensed phase particles of $Al_2O_3$, an SRM exhaust plume at high altitude may contain a significant concentration of soot particles. Soot is produced during the

combustion process in a wide range of chemical-propellant rocket propulsion systems and is thought to appear primarily as a result of local chemical nonequilibrium within reacting flow regions [1]. Because of the complex nature of soot formation and a general lack of understanding for the relevant physical processes, much uncertainty exists in the characterization of soot as part of the flowfield simulation and radiation analysis of SRM plume flows. However, experimental measurements in a high-altitude test chamber have shown a relatively high soot content in off-axis regions of a SRM exhaust plume [29]. Soot has been incorporated into detailed models for the simulation of low-altitude SRM plume flows [30], but an extensive literature search revealed no efforts at the simulation of high-altitude SRM plumes that include consideration of soot radiation.

In both experimental and numerical radiation studies for liquid-propellant rocket plumes, soot is often cited as a major contributor to plume emission characteristics [1,31,32]. To evaluate the potential contribution of soot to radiation properties for the solid-propellant plume flows of interest, additional simulations are run for the BSUV-2 flow in which soot is included as an additional particle species. In particular, we hope to determine the effect of soot on calculated UV radiance values at the onboard sensor so that the influence of soot particles on the discrepancy between experimental and numerical results may be quantitatively evaluated.

Based on previous simulations and experimental measurements of soot concentrations in exhaust flows from liquid-propellant rocket engines [1,31], we assume a 2% mass loading of soot at the nozzle exit. Although no corresponding data can be found for an SRM exhaust flow, the 2% value represents a reasonable (although very rough) estimate of the expected soot concentration in the simulated flowfield. We assume for simplicity that the soot concentration is uniform over the nozzle exit plane, and soot particles are given initial temperatures and velocities that are identical to those used for the gas. Although noticeable soot velocity and temperature lags may exist in some regions within the nozzle, the very small mass and heat capacity of soot particles allows these particles to rapidly equilibrate to local gas properties in the plume. The approximation of full equilibration at the nozzle exit should therefore have little or no impact on plume radiation or flowfield properties.

Following the expected soot particle size distribution given by Simmons [1], all soot particles are given a diameter of 0.04 $\mu$m. Input parameters for the radiation model include wavelength-and temperature-dependent values of both the refractive and absorption indices, based on an analysis of experimental data also compiled by Simmons [1].

For inclusion of soot in the radiation model, all procedures are nearly identical to those used for $Al_2O_3$ particles [21]. The only exception is in the calculation of spectral emissivity $\varepsilon_\lambda$; the correlation of Reed and Calia [2] rearranged here as Eq. (1) is not valid for use with soot, and n alternate expression must be found for use in determining soot particle emission and absorption properties. As a starting point, Mie theory gives the following expression [1,33] for the spectral absorptance $\alpha_\lambda$ at a wavelength $\lambda$ for particles of radius $R_p < \lambda/2\pi$:

$$\alpha_\lambda = \frac{36 \times 10^{-4} \pi n k}{(n^2 - k^2 + 2)^2 + 4n^2k^2} \cdot \frac{f_v}{\lambda} \tag{2}$$

where $k$ is the particle absorption index, $n$ is the refractive index ($n + ki$ is the complex index of refraction at the wavelength $\lambda$), and $f_v$ is the particle volume fraction, defined as the product of the particle number density $n_p$ and the volume per particle $4/3\pi R_p^3$. [Note that Eq. (2) differs from the formula provided by Simmons [1] and Plastinin et al. [33] in the inclusion of the factor $10^{-4}$. This factor is required so that $\alpha_\lambda \cdot \lambda$ will be a nondimensional quantity. In both of the references mentioned, $\alpha_\lambda$ is given in cm$^{-1}$, whereas $\lambda$ has units of $\mu$m.] The spectral absorptance may also be given as the product of the particle absorption cross section and number density $n_p$:

$$\alpha_\lambda = \pi R_p^2 \varepsilon_\lambda n_p \tag{3}$$

By equating the right-hand sides of Eqs. (2) and (3) to be equal, we can express the spectral emissivity $\varepsilon_\lambda$ as a function of the nondimensional ratio $R_p/\lambda$:

$$\varepsilon_\lambda = \frac{48 \times 10^{-4} \pi n k}{(n^2 - k^2 + 2)^2 + 4n^2k^2} \cdot \frac{R_p}{\lambda} \tag{4}$$

Equation (4) may then be used in radiation modeling procedures to determine emission and absorption characteristics of soot particles.

Two additional simulations are performed to assess the potential influence of soot in the BSUV-2 flow. The first simulation includes soot among the exhaust products as described earlier and is in all other ways identical to the base simulation. In the second simulation, $Al_2O_3$ particles are entirely removed so that the contribution of soot to plume radiation characteristics may be independently evaluated. Note, however, that the second simulation neglects any effects of soot absorption and scattering on radiation emitted by $Al_2O_3$ particles, and so the removal of $Al_2O_3$ particles allows for only an approximate assessment of the influence of soot.

The variation in net radiative energy flux along the extraction line is shown in Fig. 17. Results are presented for the base simulation, the simulation involving both soot and $Al_2O_3$ particles, and the simulation in which only soot particles are included. In comparing results between the first two simulations, we find that soot has a very small effect on the net energy flux over the entire length of the extraction line. When soot particles are considered independently, the total radiation intensity is found to be about 35% lower around the nozzle exit and over two orders of magnitude lower at a distance of about 75 m downstream.

The divergence in simulation results with downstream distance can be traced in part to the large difference in temperature gradients between soot and $Al_2O_3$ particles, due to convective heat transfer in the near-field plume region. As mentioned in the discussion of Fig. 4, particle temperature in the plume is generally a strong function of particle size, due to the scaling relation between heat capacity and the convective heat transfer rate. Soot particles will therefore cool far more rapidly than the much larger $Al_2O_3$ particles through energy exchange with the surrounding gas. Thermal radiation intensity scales with roughly the fourth power of the source temperature so that the downstream increase in the average temperature difference between soot and $Al_2O_3$ particles corresponds to a far larger difference in radiation intensity contributions from the two types of particles.

Another factor in the downstream increase in differences between simulation results shown in Fig. 17 is the influence of nozzle searchlight emission. As observed in Fig. 15, the relative contribution of searchlight emission to the radiative energy flux

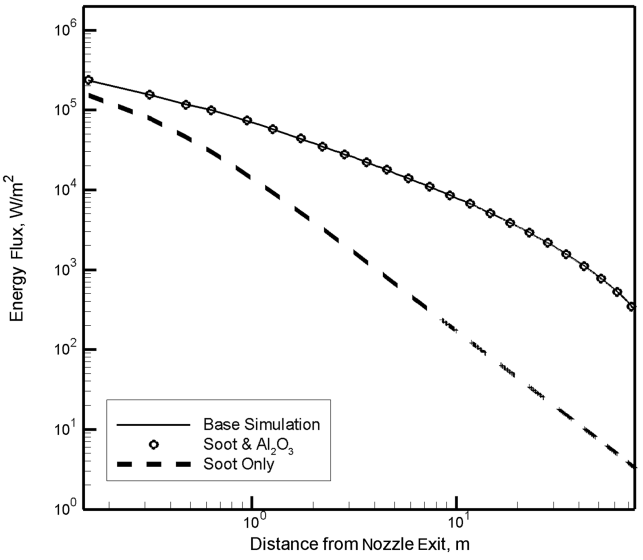


**Fig. 17 Effect of soot on the net radiative energy flux along the extraction line.**

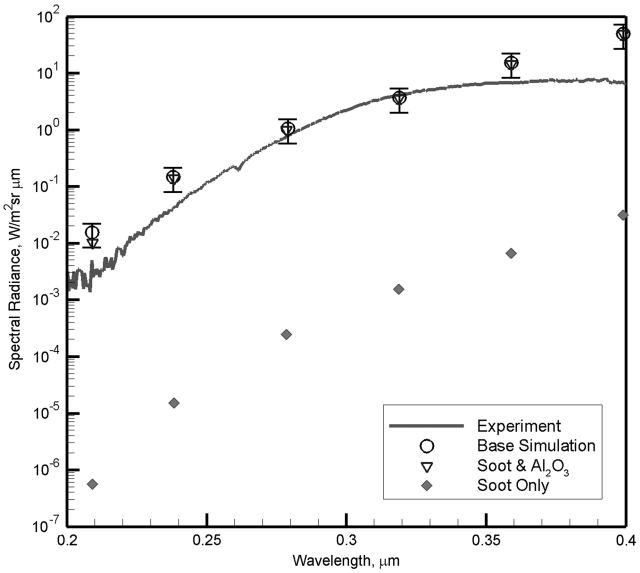


**Fig. 18 Effect of soot on UV radiance at the onboard sensor.**

decreases continuously with distance from the nozzle exit, and so particle emission and absorption play a comparatively larger role with increasing downstream distance. Searchlight emission has equal intensity for all three simulations considered here, and so we expect that differences among these simulations in particle radiation characteristics will result in a downstream increase in the variation between calculated energy-flux values.

Figure 18 shows profiles of the plume UV spectral radiance, as measured at the onboard sensor for the base simulation and the two simulations that include soot. By comparing results from these simulations with the experimental values also shown in the figure, we can roughly assess the expected contribution of soot to the discrepancy between experiment and simulation results. An examination of Fig. 18 reveals that for this particular flow and for the estimated soot concentration used here, soot has no significant influence on the calculated UV radiance values. All differences between radiance values for the base simulation and those for the simulation involving both soot and $Al_2O_3$ particles are within the error bars for statistical scatter, and values for the simulation that includes only soot are uniformly over four orders of magnitude lower.

The fact that soot has such a small effect on plume UV radiance can be attributed to the very small soot mass loading used in the simulations (less than 7% of that of $Al_2O_3$ particles) and particularly to the large difference between soot and $Al_2O_3$ particle temperatures throughout the plume. Note that thermal radiation intensity in the UV range is particularly sensitive to source particle temperatures, whereas most of the radiative energy flux throughout the simulated flowfield is concentrated at IR wavelengths for which thermal radiative emission is a weaker function of temperature. The relative contribution of soot is therefore found to be far smaller in Fig. 18 than in the net radiative energy-flux values displayed in Fig. 17.

## VIII. Conclusions

The simulation of high-altitude exhaust plumes from solid-propellant rockets presents a number of modeling difficulties and involves consideration of several complex physical processes that are not entirely understood. The work presented here was performed with the goal of advancing the current state of modeling capabilities for these flows and assessing the relative influence and interaction between potentially important phenomena. Although the simulation scheme described earlier does not resolve many of the known sources of inaccuracy in the simulation of high-altitude SRM plume flows [2], it does address several physical flow processes that have received little previous attention in the literature and allows these processes to be considered together within a unified numerical framework.

In an effort to evaluate the overall accuracy of the proposed scheme, a series of simulations was performed for a representative SRM plume flow. Comparisons were made between calculated UV radiance values and measured values from a flight experiment. Although no definite conclusions could be drawn from these comparisons, relatively good agreement was observed between simulation and experimental results. Note that a rigorous assessment of simulation accuracy is not possible due a lack of more detailed experimental data, although the level of agreement observed here is an encouraging indication of overall accuracy.

A series of parametric studies involving simulations of the same SRM plume flow were used to evaluate the influence of several physical processes and input parameters. The first of these studies considered models for gas–particle interaction. Here, we found that particle and gas temperatures through much of the plume may be significantly affected by two-way interphase momentum and energy exchange. Values of the particle thermal accommodation coefficient were found to greatly influence flowfield properties, as well as radiation intensity in the far-field plume region, whereas effects of particle rotation were shown to be negligible.

Another study examined models and parameters related to plume radiation. Here, we found that only the choice of particle UV absorption index values can account for the discrepancy observed between simulation and experimental values of plume spectral radiance in the 0.2- to 0.25-$\mu$m wavelength range. Most of the disagreement with the experimental data can therefore be traced to a large inherent uncertainty in the determination of absorption index values. Within the IR range, these values were also found to strongly influence particle temperatures and net radiation intensity through much of the plume. Nozzle searchlight emission was shown to significantly contribute to net radiation intensity in the near-field plume region, whereas particle radiative emission (but not absorption) was observed to have a considerable effect on particle temperatures further downstream.

A third parametric study considered the potential influence of soot on plume radiation properties. Soot was found to have a very small effect on net radiation intensity throughout the plume, with a contribution relative to that of $Al_2O_3$ particles that decreases continuously with downstream distance. As measured from a simulated onboard sensor, UV spectral radiance values associated with soot are roughly four orders of magnitude smaller than base simulation values, and so the presence of soot may be safely ruled out as a significant contributor to the differences observed between simulation results and experimental data.

## Acknowledgments

The authors gratefully acknowledge the U.S. Air Force Research Laboratory at Edwards Air Force Base for financial support of this work, with Tom Smith as technical monitor.

## References

[1] Simmons, F. S., *Rocket Exhaust Plume Phenomenology*, Aerospace Press, El Segundo, CA, 2000.

[2] Reed, R. A., and Calia, V. S., "Review of Aluminum Oxide Rocket Exhaust Particles," AIAA Paper 93-2819, 1993.

[3] York, B. J., Lee, R. A., Sinha, N., and Dash, S. M., "Progress in the Simulation of Particulate Interactions in Solid Propellant Rocket Exhausts," AIAA Paper 2001-3590, 2001.

[4] Dash, S. M., Wolf, D. E., Beddini, R. A., and Pergament, H. S., "Analysis of Two-Phase Flow Processes in Rocket Exhaust Plumes," *Journal of Spacecraft and Rockets*, Vol. 22, No. 3, 1985, pp. 367–380.

[5] Chen, C. L., Ramakrishnan, S., Ota, D. K., Rajagopal, K., and Wisneski, J., "Computation of Underexpanded Solid Rocket Plume and Its Effects on the Mated Shuttle Configuration," AIAA Paper 92-2612, 1992.

[6] Rattenni, L., "Solid Motor Plume Analysis for the STAR-1 Spacecraft," AIAA Paper 2000-3190, 2000.

[7] Clark, M. S., Fisher, S. C., and French, E. P., "The Flow of Very Small Alumina Particles in a Solid Rocket Plume," AIAA Paper 81-1384, 1981.

[8] Hueser, J. E., Melfi, L. T., Bird, G. A., and Brock, F. J., "Analysis of Large Solid Propellant Rocket Exhaust Plumes Using the Direct Simulation Monte Carlo Method," AIAA Paper 84-0496, 1984.
[9] Bird, G. A., *Molecular Gas Dynamics and the Direct Simulation of Gas Flows*, Clarendon Press, Oxford, 1994.
[10] Candler, G. V., Levin, D. A., Brandenburg, J., Collins, R., Erdman, P., Zipf, E., and Howlett, C., "Comparison of Theory with Plume Radiance Measurements from the Bow Shock Ultraviolet 2 Rocket Flight," AIAA Paper 92-0125, 1992.
[11] Anfimov, N. A., Karabadjak, G. F., Khmelinin, B. A., Plastinin, Y. A., and Rodinov, A. V., "Analysis of Mechanisms and Nature of Radiation from Aluminum Oxide in Different Phase States in Solid Rocket Exhaust Plumes," AIAA Paper 93-2818, 1993.
[12] Vitkin, E. I., Karelin, V. G., Kirillov, A. A., Suprun, A. S., and Knadyka, J. V., "A Physico-Mathematical Model of Rocket Exhaust Plumes," *International Journal of Heat and Mass Transfer*, Vol. 40, No. 5, 1997, pp. 1227–1241. doi:10.1016/0017-9310(96)00140-8
[13] Alexeenko, A. A., Wadsworth, D. C., Gimelshein, S. F., and Ketsdever, A. D., "Numerical Modeling of ISS Thruster Plume Induced Contamination Environment," *Optical Systems Degradation, Contamination, and Stray Light: Effects, Measurements, and Control*, Proceedings of SPIE—the International Society for Optical Engineering, Vol. 5526,Society of Photo-Optical Instrumentation Engineers, Bellingham, WA, 2004, pp. 125–136.
[14] Gimelshein, S. F., Alexeenko, A. A., Wadsworth, D. C., and Gimelshein, N. E., "The Influence of Particulates on Thruster Plume/Shock Layer Interaction at High Altitudes," AIAA Paper 2005-766, 2005.
[15] Gimelshein, S. F., Markelov, G., and Muylaert, J., "Numerical Modeling of Low Thrust Solid Propellant Nozzles at High Altitudes," AIAA Paper 2006-3273, 2006.
[16] Gallis, M. A., Torczynski, J. R., and Rader, D. J., "An Approach for Simulating the Transport of Spherical Particles in a Rarefied Gas Flow via the Direct Simulation Monte Carlo Method," *Physics of Fluids*, Vol. 13, No. 11, 2001, pp. 3482–3492. doi:10.1063/1.1409367
[17] Gimelshein, N. E., Lyons, R. B., Reuster, J. G., and Gimelshein, S. F., "Numerical Prediction of UV Radiation from Two-Phase Plumes at High Altitudes," AIAA Paper 2007-1014, 2007.
[18] Burt, J. M., and Boyd, I. D., "Development of a Two-Way Coupled Model for Two Phase Rarefied Flows," AIAA Paper 2004-1351, 2004.
[19] Burt, J. M., and Boyd, I. D., "Particle Rotation Effects in Rarefied Two Phase Plume Flows," *24th International Symposium on Rarefied Gas Dynamics*, Vol. 762, American Inst. of Physics, Melville, NY, May 2005, pp. 413–418.
[20] Burt, J. M., and Boyd, I. D., "Monte Carlo Simulation of a Rarefied Multiphase Plume Flow," AIAA Paper 2005-0964, 2005.
[21] Burt, J. M., and Boyd, I. D., "A Monte Carlo Radiation Model for Simulating Rarefied Multiphase Plume Flows," AIAA Paper 2005-4691, 2005.
[22] Erdman, P. W., Zipf, E., Espy, P., Howlett, C., Levin, D. A., and Candler, G. V., "In-Situ Measurements of UV and VUV Radiation from a Rocket Plume and Re-Entry Bow Shock," AIAA Paper 92-0124, 1992.
[23] Breuer, K. S., Piekos, E. S., and Gonzales, D. A., "DSMC Simulations of Continuum Flows," AIAA Paper 95-2088, 1995.
[24] Burt, J. M., and Boyd, I. D., "Evaluation of a Particle Method for the Ellipsoidal Statistical Bhatnagar-Gross-Krook Equation," AIAA Paper 2006-0989, 2006.
[25] Boyd, I. D., Chen, G., and Candler, G. V., "Predicting Failure of the Continuum Fluid Equations in Transitional Hypersonic Flows," *Physics of Fluids*, Vol. 7, No. 1, 1995, pp. 210–219. doi:10.1063/1.868720
[26] Konopka, W. L., Reed, R. A., and Calia, V. S., "Measurements of Infrared Optical Properties of $Al_2O_3$ Rocket Particles," AIAA Paper 83-1568, 1983.
[27] Siegel, R., and Howell, J. R., *Thermal Radiation Heat Transfer*, Hemisphere, Washington, DC, 1981.
[28] Reed, R. A., Beale, K. S., Neese, D. W., Sherrell, F. G., Roberds, D. W., and Oliver, S. M., "The Effect of Seachlight Emission on Radiation from Solid Rocket Plumes," AIAA Paper 92-2918, 1992.
[29] Girata, P. T., and McGregor, W. K., "Particle Sampling of Solid Rocket Motor (SRM) Exhausts in High Altitude Test Cells," AIAA Paper 83-245, 1983.
[30] Plastinin, Y. A., Karabadzhak, G., and Khmelinin, B., "Ultraviolet, Visible and Infrared Spectra Modeling for Solid and Liquid-Fuel Rocket Exhausts," AIAA Paper 2001-660, 2001.
[31] Wright, M. J., Rao, R. M., Candler, G. V., Hong, J. S., Schilling, T. A., and Levin, D. A., "Modeling Issues in the Computation of Plume Radiation Signatures," AIAA Paper 98-3622, 1998.
[32] Garrison, M., Ozawa, T., and Levin, D. A., "An Improved $CO_2$, $H_2O$ and Soot Infrared Radiation Models for High Temperature Flows," AIAA Paper 2005-4777, 2005.
[33] Plastinin, Y., Karabadzhak, G., Khmelinin, B., Baula, G., and Rodionov, A., "Advanced Model for Soot Radiation in the Plume," AIAA Paper 2002-798, 2002.

J. Gore
*Associate Editor*